particles

MDPI

Article

Hyperon Production in Bi + Bi Collisions at the Nuclotron-Based Ion Collider Facility and Angular Dependence of Hyperon Spin Polarization

Nikita S. Tsegelnik [1], Vadym Voronyuk [2] and Evgeni E. Kolomeitsev [1,3,*]

[1] Laboratory of Theoretical Physics, Joint Institute for Nuclear Research, RU-141980 Dubna, Russia; tsegelnik@jinr.ru
[2] Laboratory of High Energy Physics, Joint Institute for Nuclear Research, RU-141980 Dubna, Russia; vadim.voronyuk@jinr.ru
[3] Department of Physics, Faculty of Natural Sciences, Matej Bel University, SK-97401 Banska Bystrica, Slovakia
* Correspondence: evgeni.kolomeitsev@umb.sk

Abstract: The strange baryon production in Bi + Bi collisions at $\sqrt{s_{NN}} = 9.0\,\text{GeV}$ is studied using the PHSD transport model. Hyperon and anti-hyperon yields, transverse momentum spectra, and rapidity spectra are calculated, and their centrality dependence and the effect of rapidity and transverse momentum cuts are studied. The rapidity distributions for $\overline{\Lambda}$, Ξ, $\overline{\Xi}$ baryons are found to be systematically narrower than for Λs. The p_T slope parameters for anti-hyperons vary more with centrality than those for hyperons. Restricting the accepted rapidity range to $|y| < 1$ increases the slope parameters by 13–30 MeV, depending on the centrality class and the hyperon mass. Hydrodynamic velocity and vorticity fields are calculated, and the formation of two oppositely rotating vortex rings moving in opposite directions along the collision axis is found. The hyperon spin polarization induced by the medium vorticity within the thermodynamic approach is calculated, and the dependence of the polarization on the transverse momentum and rapidity cuts and on the centrality selection is analyzed. The cuts have stronger effect on the polarization of Λ and Ξ hyperons than on the corresponding anti-hyperons. The polarization signal is maximal for the centrality class, 60–70%. We show that, for the considered hyperon polarization mechanism, the structure of the vorticity field makes an imprint on the polarization signal as a function of the azimuthal angle in the transverse momentum plane, ϕ_H, $\cos\phi_H = p_x/p_T$. For particles with positive longitudinal momentum, $p_z > 0$, the polarization increases with $\cos\phi_H$, while for particles with $p_z < 0$ it decreases.

Keywords: heavy-ion collisions; hydrodynamics; vorticity; hyperon polarization; vortex rings; dynamical freeze-out; NICA; PHSD; MPD

check for updates

Citation: Tsegelnik, N.S.; Voronyuk, V.; Kolomeitsev, E.E. Hyperon Production in Bi + Bi Collisions at the Nuclotron-Based Ion Collider Facility and Angular Dependence of Hyperon Spin Polarization. *Particles* **2024**, *7*, 984–1003. https://doi.org/10.3390/particles7040060

Academic Editor: Peter Senger

Received: 26 September 2024
Revised: 3 November 2024
Accepted: 11 November 2024
Published: 13 November 2024

Copyright: © 2024 by the authors. Licensee MDPI, Basel, Switzerland. This article is an open access article distributed under the terms and conditions of the Creative Commons Attribution (CC BY) license (https://creativecommons.org/licenses/by/4.0/).

1. Introduction

The global spin polarization of hyperons has been measured in heavy-ion collisions (HICs) in the broad energy range from several TeV at LHC [1] to a few GeV at SIS [2]. The polarization signal increases with decreasing energy, reaching a maximum at center-of-mass energies around $\sqrt{s_{NN}} = 3\,\text{GeV}$. A remarkable feature of the hyperon polarization is that $\overline{\Lambda}$s are more strongly polarized than Λs [3]. This is in striking contrast to hyperon polarization in proton–proton and proton–nucleus collisions, where the anti-hyperons do not gain any polarization [4]. Therefore, another mechanism is operative in HICs [5,6]. Several such mechanisms have been proposed in the literature; see review [7]. The statistical approach developed in [8–11] suggests that the local spin polarization of fermions arises due to the local vorticity gained by the fireball medium due to the initial angular momentum of the colliding nuclei. Implemented in hydrodynamic [12–17] and transport models [18–23], this mechanism allows us to reproduce the measured Λ polarization, except for the low energy HADES data; see Figure 3 in [2]. On the other hand, the splitting

between $\overline{\Lambda}$ and Λ polarization signals cannot be reproduced in most works unless a special mechanism distinguishing particles from anti-particles is introduced [17,24,25]. Within the transport approach, the splitting was reproduced in the UrQMD model [23] and in the PHSD model [26]. The origin of the splitting is discussed in detail in Ref. [27].

The Multi-Purpose Detector (MPD) is the flagship heavy-ion experiment to be built at the Nuclotron-based Ion Collider Facility (NICA) at JINR (Dubna) in the center-of-mass energy range $\sqrt{s_{NN}} = 4$–11 GeV [28]. It is well suited for the identification of strange particles [29]. Recently, it has been shown that the MPD detector system is able to reconstruct the global Λ polarization [30].

In this paper, we consider the strange particle production and the formation of the polarization signal in the collision Bi + Bi at $\sqrt{s_{NN}} = 9.0$ GeV. The potential of the MPD for studying this colliding system was previously outlined in Ref. [31]. We demonstrate that the vortical mechanism of the hyperon polarization makes a particular impact on the dependence of hyperon polarization on its momentum. We use the Parton-Hadron-String Dynamics (PHSD) transport model [32,33], which was extended [34] for the determination of the vorticity field in the fluidized hot and dense subsystem of interacting particles (participants). As shown in Refs. [26,27], it is possible to reproduce the measured global Λ polarization in collisions at $\sqrt{s_{NN}} = 7.7$ and 11.5 GeV and the global $\overline{\Lambda}$ polarization at 11.5 GeV.

In Section 2, we define a criterion for the selection of centrality classes and present our results of hyperon yields and their rapidity and transverse momentum distributions. In Section 3, we calculate the hyperon polarization and examine the dependence of the polarization signal for various hyperon species on the transverse momentum and rapidity cuts. Furthermore, we examine the centrality dependence of the hyperon polarization signals. In Section 4, we investigate the correlations between the hyperon polarization signal and its momentum. Conclusions are formulated in Section 5.

2. Hyperon Multiplicities and Spectra

Since we deal with finite nuclear systems with a non-homogenous density distribution in HICs, the results of any measured observables depend on the initial geometry. The initial energy/entropy content of the nucleus overlap zone crucially determines final particle multiplicities and momenta distribution and/or energy, measured in the forward rapidity region, which is sensitive to spectator fragments. Therefore, to gain a better understanding of the processes in HICs and constrain model parameters, one is interested in selection of the initial configuration of colliding nuclei cast, e.g., in terms of the impact parameter b, or mediate quantities such as the number of nucleon collisions $N_{\rm coll}$ and the number of participating nucleons $N_{\rm part}$.

In experimental studies, collisions are grouped into event (centrality) classes when the most central class includes the events with the highest multiplicity of secondary particles (smallest forward energy), which correspond to small values of the impact parameter.

For the centrality determination, one constructs the event distribution of charged particles, $\frac{{\rm d}N_{\rm ev}}{{\rm d}N_{\rm ch}}$, using some microscopic model of a collision or the Glauber Monte Carlo method [35], and then defines the centrality classes as a fraction of the total integral

$$C = \frac{1}{N_{\rm ev}} \int_0^{N_{\rm ch}} \frac{{\rm d}N_{\rm ev}}{{\rm d}N_{\rm ch}} {\rm d}N_{\rm ch}. \quad (1)$$

Finally, the geometric parameters, such as the impact parameter, b, the number of participants, $N_{\rm part}$, and the number of binary nucleon–nucleon collisions can be estimated for each centrality class. The standard experimental procedure is described, for instance, in Refs. [36–39]. In Refs. [40,41] another method for the centrality class selection was proposed, which requires only a conjecture of the conditional probability distribution of $N_{\rm ch}$ for the fixed impact parameter b. The gamma-distribution was suggested in Ref. [41] to be used for the probability $P(N_{\rm ch}|b)$. This approach is also applied for the centrality determination in the BM@N experiment at NICA [42,43]. As pointed out in Ref. [44], the

centrality determination could be influenced by the detector acceptance (for most central collisions) and by the spectator fragmentation.

Using the PHSD model, we generated about $N_{ev}^{tot} \simeq 2 \times 10^6$ events. The distribution of the number of charged particles, N_{ch}, with the pseudorapidity range $|\eta| < 0.5$ is shown in Figure 1. We define the centrality classes using the procedure similar to the traditional experimental one (1). The division in centrality classes is presented in Figure 1. We also show the corresponding number of participants N_{part} and impact parameter for certain N_{ch}.

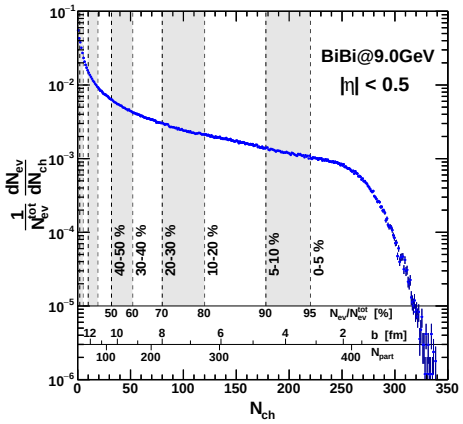


Figure 1. The multiplicity histogram for charged particles N_{ch} in the middle pseudorapidity region $|\eta| < 0.5$ in the Bi + Bi collisions at $\sqrt{s_{NN}} = 9.0$ GeV simulated within the PHSD model. The centrality classes shown by vertical lines are determined using a part of the total integral of the histogram; see Equation (1). Two additional internal scales are displayed on the plot, indicating the number of participants, N_{part}, and the impact parameter, b, of the collision.

The PHSD transport model was developed to reproduce the observed strange particle multiplicities in the broad range of collision energies [32,45–47]. In-medium modifications of kaon properties were needed to understand the strangeness production at SIS energies, $\sqrt{s_{NN}} \simeq$ 2–3 GeV. For higher collision energies (in the SPS and RHIC energy range), another mechanism is implemented in the description of initial hard processes taken as in the FRITIOF Lund model [48,49], which utilizes the Schwinger mechanism for the quark–anti-quark pair production in string decays. References [46,47] suggested in-medium modifications of the quark masses due to a decrease in the quark condensate magnitude when the string breaking occurs in the dense and hot medium created in collisions. This leads to an increase in the probability of the strangeness production. Within the PHSD code, the values of quark condensate are calculated in each cell on each time step. These modifications of the string-breaking processes lead to significant improvements in the description of strange particle production at AGS and SPS energies [46,47].

In Figure 2, we present multiplicities of hyperons and anti-hyperons (i.e., averaged number of particles per event, N_H / N_{ev}^{tot}) with and without experimental p_T, and rapidity cuts for various centrality classes. Calculations show that the results for the minimum bias collisions correspond to the centrality class 30–40%. The multiplicity drops exponentially with a centrality increase, i.e., for larger impact parameters and more peripheral collisions. So, the minimum bias multiplicities are, on average, 3.3 times smaller than for the most central collisions of the 0–10% centrality class. For the most central collisions with the 0–5% centrality class, we have the following relations among yields of hyperons with the various strangeness contents:

$$M_\Lambda : M_\Xi : M_\Omega = 1 : (9.10 \pm 0.02) \times 10^{-2} : (3.71 \pm 0.04) \times 10^{-3},$$
$$M_{\overline{\Lambda}} : M_{\overline{\Xi}} : M_{\overline{\Omega}} = 1 : (2.09 \pm 0.02) \times 10^{-1} : (2.16 \pm 0.06) \times 10^{-2}. \quad (2)$$

This hierarchy of yields can be compared with the results of the NA49 experiment on central (0–7%) Pb + Pb collision at $\sqrt{s_{NN}} = 8.77\,\text{GeV}$ reported in Refs. [50,51]

$$M_\Lambda : M_\Xi : M_\Omega = 1 : (7 \pm 1) \times 10^{-2} : (3 \pm 2) \times 10^{-3}\,,$$
$$M_{\overline{\Lambda}} : M_{\overline{\Xi}} = 1 : (2 \pm 0.5) \times 10^{-1}. \quad (3)$$

There is a good overall agreement between our calculations (2) and the experimental finding for collisions of nuclei with similar A and similar collision energies.

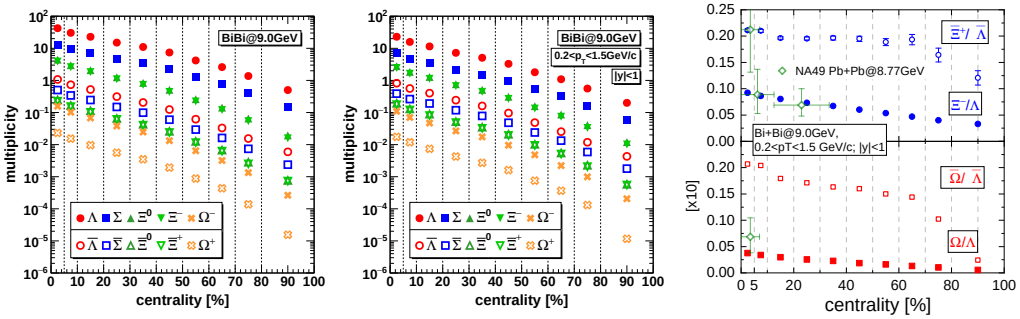


Figure 2. Hyperon multiplicities for various centrality classes in Bi + Bi collisions at $\sqrt{s_{NN}} = 9.0\,\text{GeV}$ without any cuts (**left panel**) and in the midrapidity region $|y| < 1$ with transverse momentum cut $0.2 < p_T < 1.5\,\text{GeV}/c$ (**middle panel**). The vertical dashed lines show the widths of the centrality bins. The minimum bias multiplicity almost coincides with one from the centrality class 30–40%. Statistical error bars are of a size of a symbol. The right panel shows the centrality dependence of the hyperon multiplicities ratios. Open diamonds correspond to the experimental ratios of hyperon multiplicities at the mid-rapidity measured by the NA49 collaboration [50,51] in Pb + Pb collisions at $\sqrt{s_{NN}} = 8.77\,\text{GeV}$ (40 AGeV beam energy).

The imposed rapidity and p_T cuts reduce the number of Λs and Σs by a factor of 0.6, Ξ hyperons by a factor of 0.7, and Ω hyperons by a factor of 0.8. The anti-hyperons are influenced by the cuts even weaker: mutiplicities of $\overline{\Lambda}$, $\overline{\Sigma}$, $\overline{\Xi}$, and $\overline{\Omega}$ are reduced by a factor of 0.9.

The relative enhancement of multi-strange particle production in central heavy-ion collisions with respect to peripheral ones has been suggested as a signature for the transient existence of a QGP phase [52]. Such a weak enhancement of the Ξ^-/Λ ratio experimentally observed in collisions at the AGS energies was analyzed in Ref. [53] within the UrQMD transport model. For the top SPS energy, the more pronounced centrality dependence of Ξ^-/Λ, Ω/Λ, $\overline{\Xi}^+/\overline{\Lambda}$, and $\overline{\Omega}/\overline{\Lambda}$ ratios was described in Ref. [54] in the framework of the QGSM model [55–57]. In the right panel of Figure 2, we show the ratios of hyperon and anti-hyperon multiplicities. For comparison, we depict in Figure 2 the ratios of experimental multiplicities measured by the NA49 collaboration in Pb + Pb collisions at $\sqrt{s_{NN}} = 8.77\,\text{GeV}$ [50,51]. We used the mid-rapidity multiplicities, for which there are some information on the centrality dependence [50]. We see in Figure 2, first, that the ratios of anti-particles is larger than the particle ratios, i.e., $\frac{\overline{\Xi}^+}{\overline{\Lambda}} > \frac{\Xi^-}{\Lambda}$ and $\frac{\overline{\Omega}}{\overline{\Lambda}} > \frac{\Omega}{\Lambda}$. Second, observation is that the anti-hyperon ratios increase very rapidly from the most peripheral to the semi-central collisions for $60\% < C < 100\%$. With a further decrease in C below 60%, all ratios grow slowly.

To clarify which of the cuts is responsible for the yield suppression to a larger expansion, we consider rapidity and p_T distributions of hyperons. Figure 3 presents the rapidity distributions of Λ and $\overline{\Lambda}$ with and without p_T cuts. Comparing plots in the left and right columns we see that the p_T cuts lead only to a moderate reduction in particle yields: by a factor of 0.86 for Λ particles and by a factor of 0.92 for $\overline{\Lambda}$. The strongest effect is caused by the rapidity cut shown in Figure 3 by vertical lines. We also observe that the influence of this cut is stronger for Λ hyperons than for $\overline{\Lambda}$, since the former one has a broader

rapidity distribution. For a more quantitative comparison of the rapidity distributions, we parameterize them by two Gaussian functions with a width σ shifted by Δy around the midrapidity,

$$\frac{\mathrm{d}N}{\mathrm{d}y} = \frac{A}{2\sqrt{2\pi\sigma^2}}\left(\exp\left[-\frac{(y-\Delta y)^2}{2\sigma^2}\right] + \exp\left[-\frac{(y+\Delta y)^2}{2\sigma^2}\right]\right). \quad (4)$$

Using this distribution, we fit the Λ and $\overline{\Lambda}$ rapidity distributions shown in Figure 3 for the centrality classes 0–5% and 30–40% in the rapidity range $-2 \le y \le 2$, and obtain the following for Λ hyperons:

$$\begin{aligned} \text{centrality class 0–5\% :} \quad & \Delta y_\Lambda = 0.72(1)\,, \quad \sigma_\Lambda = 0.74(2)\,, \quad A_\Lambda = 44 \pm 0.5\,, \\ \text{centrality class 30–40\% :} \quad & \Delta y_\Lambda = 0.91(1)\,, \quad \sigma_\Lambda = 0.82(3)\,, \quad A_\Lambda = 12 \pm 0.2\,, \end{aligned} \quad (5)$$

and for $\overline{\Lambda}$ hyperons:

$$\begin{aligned} \text{centrality class 0–5\% :} \quad & \Delta y_{\overline{\Lambda}} = 0.41(1)\,, \quad \sigma_{\overline{\Lambda}} = 0.49(1)\,, \quad A_{\overline{\Lambda}} = 1.08 \pm 0.01\,, \\ \text{centrality class 30–40\% :} \quad & \Delta y_{\overline{\Lambda}} = 0.39(1)\,, \quad \sigma_{\overline{\Lambda}} = 0.46(1)\,, \quad A_{\overline{\Lambda}} = 0.206 \pm 0.001. \end{aligned} \quad (6)$$

We see that the rapidity distributions of $\overline{\Lambda}$ are significantly narrower than those for Λ, i.e., $\Delta y_{\overline{\Lambda}} < \Delta y_\Lambda$ and $\sigma_{\overline{\Lambda}} < \sigma_\Lambda$. Another interesting difference between hyperons and anti-hyperons is that the Λ y-distributions for 30–40% centrality is broader than that for 0–5% centrality: $\Delta y_\Lambda[0\text{–}5\%] < \Delta y_\Lambda[30\text{–}40\%]$ and $\sigma_\Lambda[0\text{–}5\%] < \sigma_\Lambda[30\text{–}40\%]$, whereas for $\overline{\Lambda}$, we observe the opposite dependence: $\Delta y_{\overline{\Lambda}}[0\text{–}5\%] > \Delta y_{\overline{\Lambda}}[30\text{–}40\%]$ and $\sigma_{\overline{\Lambda}}[0\text{–}5\%] > \sigma_{\overline{\Lambda}}[30\text{–}40\%]$.

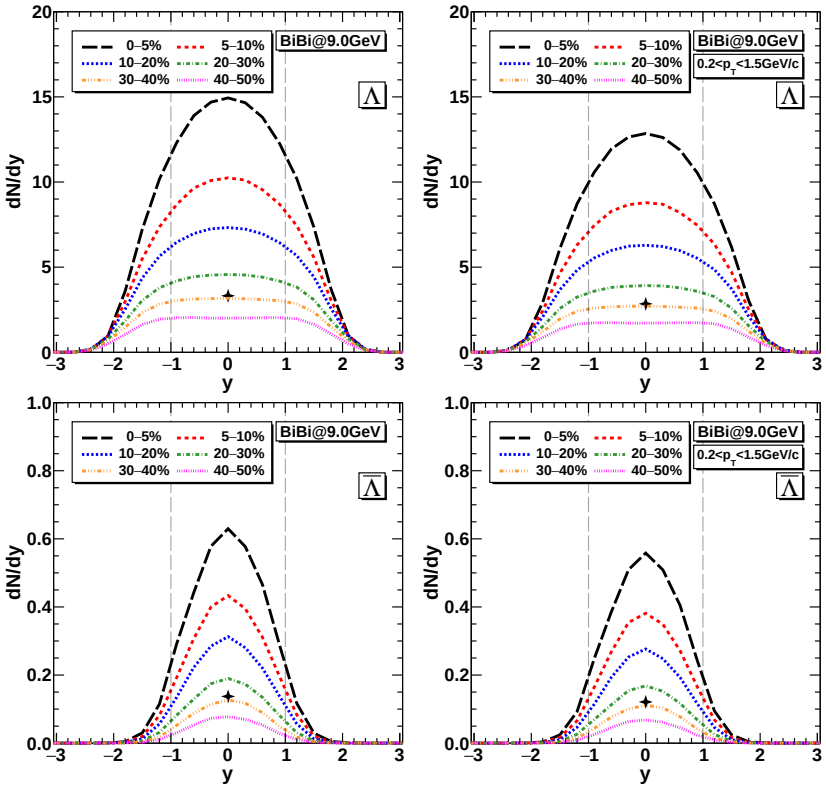


Figure 3. Rapidity distribution of Λ hyperons (**upper row**) and $\overline{\Lambda}$ hyperons (**lower row**) without momentum cuts (**left**) and with the transverse momentum cut $0.2 < p_T < 1.5\,\mathrm{GeV}/c$ (**right**). The minimum bias value $dN/dy|_{y=0}$ is shown by a star. The statistical uncertainty of the calculations is comparable with the line width.

In Figure 4, we show the rapidity distributions of Ξ and $\overline{\Xi}$ hyperons. Fitting these distributions with Equation (4), we find, for Ξ hyperons,

$$\begin{aligned} \text{centrality class 0–5\%}: &\quad \Delta y_{\Xi} = 0.55(1)\,, \quad \sigma_{\Xi} = 0.65(2)\,, \quad A_{\Xi} = 3.91 \pm 0.04, \\ \text{centrality class 30–40\%}: &\quad \Delta y_{\Xi} = 0.59(1)\,, \quad \sigma_{\Xi} = 0.67(2)\,, \quad A_{\Xi} = 0.736 \pm 0.006, \end{aligned} \tag{7}$$

and for $\overline{\Xi}$ hyperons,

$$\begin{aligned} \text{centrality class 0–5\%}: &\quad \Delta y_{\overline{\Xi}} = 0.38(1)\,, \quad \sigma_{\overline{\Xi}} = 0.47(1)\,, \quad A_{\overline{\Xi}} = 0.226 \pm 0.001, \\ \text{centrality class 30–40\%}: &\quad \Delta y_{\overline{\Xi}} = 0.37(1)\,, \quad \sigma_{\overline{\Xi}} = 0.42(2)\,, \quad A_{\overline{\Xi}} = 0.040 \pm 0.001. \end{aligned} \tag{8}$$

Hence, the Ξ rapidity distributions are narrower than those for Λs, whereas the $\overline{\Xi}$ distributions are similar to those for $\overline{\Lambda}$. Remarkably, both Ξ and $\overline{\Xi}$ distributions depend very weakly on centrality.

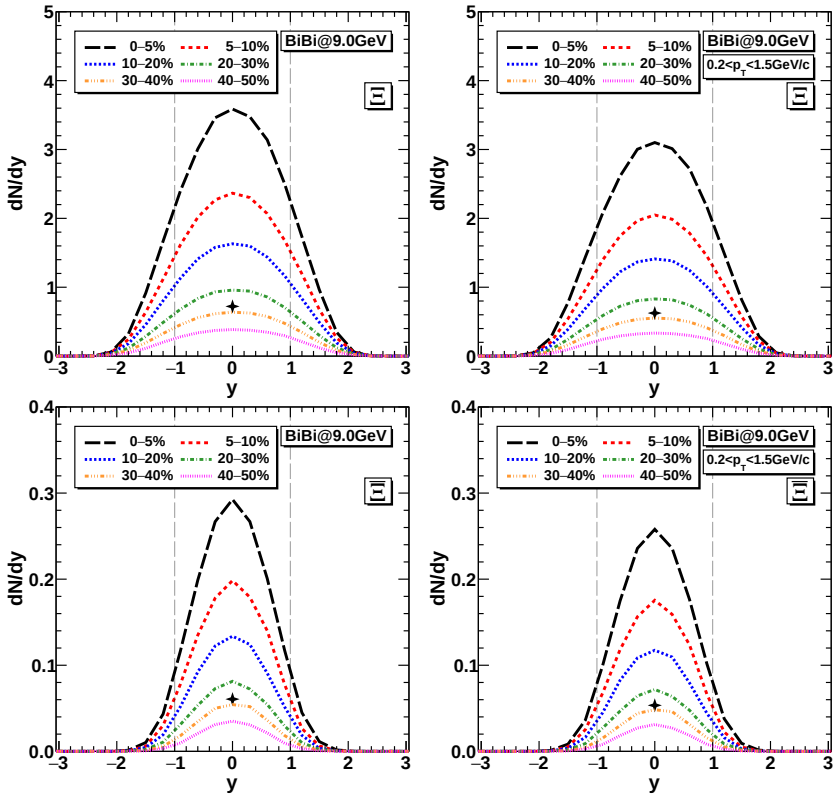


Figure 4. The same as in Figure 3, but for Ξ and $\overline{\Xi}$ hyperons.

In Ref. [27], we showed that the PHSD code can reproduce the p_T spectra of Λs measured by the STAR collaboration in Au + Au collisions [58] at $\sqrt{s_{NN}} = 7.7$ GeV. In Ref. [26] the excitation functions of the hyperon multiplicities are confronted with available data for AGS, SPS, and RHIC energies. Further comparisons of the PHSD code with the experimental data can be found in [46,47]. For the Bi + Bi collisions at 9.0 GeV we consider here the transverse momentum spectra of Λ and $\overline{\Lambda}$ hyperons are depicted in Figure 5, and the spectra of Ξ and $\overline{\Xi}$ hyperons in Figure 6. For momenta below 1.5 GeV, the statistical uncertainty is of the size of the line width, but it increases for higher momenta, as follows from the line oscillations especially for anti-hyperons. The magnitudes of the spectra are reflected in the total hyperon multiplicities discussed above; see Figure 2.

To quantify the slopes of the spectra we fit them in the momentum interval $0.5 \leq p_T \leq 1.5$ GeV with the blast-wave formula [59,60],

$$\frac{\mathrm{d}N}{2\pi p_T \mathrm{d}p_T} = A m_T K_1\left(m_T/T_{\mathrm{slope}}\right), \quad m_T = \sqrt{m_H^2 + p_T^2}, \tag{9}$$

for spectra without the rapidity cut. For spectra with the rapidity cut $|y| \leq 1$. we would have to use expression

$$\frac{\mathrm{d}N}{2\pi p_T \mathrm{d}p_T} = A m_T \int_0^1 \mathrm{d}y \cosh y \exp\left(\frac{m_T}{T_{\mathrm{slope}}} \cosh y\right). \tag{10}$$

However, for the typical parameters $T_{\mathrm{slope}} \sim 150$–$200$ MeV, Functions (9) and (10) differ by less than 1%, so we can use Equation (9). We should emphasize that the simple parameterization above can be used only for rather narrow momentum intervals. For a broader interval including low and high p_T parts, combinations of several distributions, like a double-temperature Boltzmann distribution together with a Tsallis–Pareto distribution, should be applied.

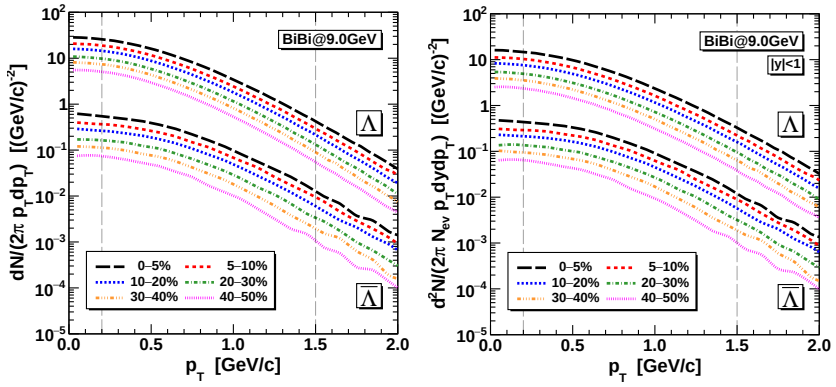


Figure 5. Transverse momentum distributions of Λ and $\overline{\Lambda}$ hyperons for different centrality classes without momentum cuts (**left panel**) and in the rapidity range $|y| < 1$ (**right panel**).

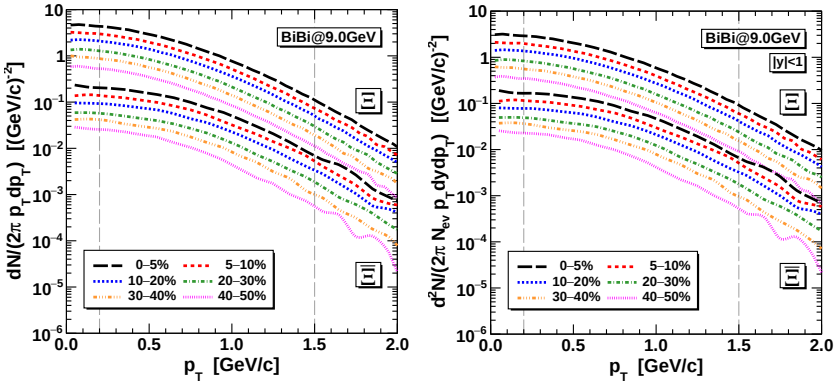


Figure 6. The same as in Figure 5, but for Ξ and $\overline{\Xi}$ hyperons.

The results of fits are presented in Figure 7. The slope parameters for Λ and Ξ hyperons show a weak dependence on the centrality monotonously decreasing by $\sim$15 MeV for Λs and $\sim$8 MeV for Ξs from the most central collisions to the 40–50% centrality class. Anti-hyperons show much stronger variations with the centrality increase by about 30 MeV from central to semi-peripheral collisions. Also, the variation is not monotonous and the slope parameter increases, first from the 0–5% centrality bin to the 5–10% bin. Comparing the left and right planes in Figure 7, we see that restricting rapidities to $|y| < 1$ leads

to an increase in the slope parameters by 13–17 MeV for Λs and by 30 MeV for Ξs. The centrality dependence of the slope parameter is similar to those without the rapidity cut. For anti-hyperons, the restriction of the rapidity range produces a smaller increase in the $T_{\rm slope}$, but enhances the non-monotonous variation of the slope parameter with centrality.

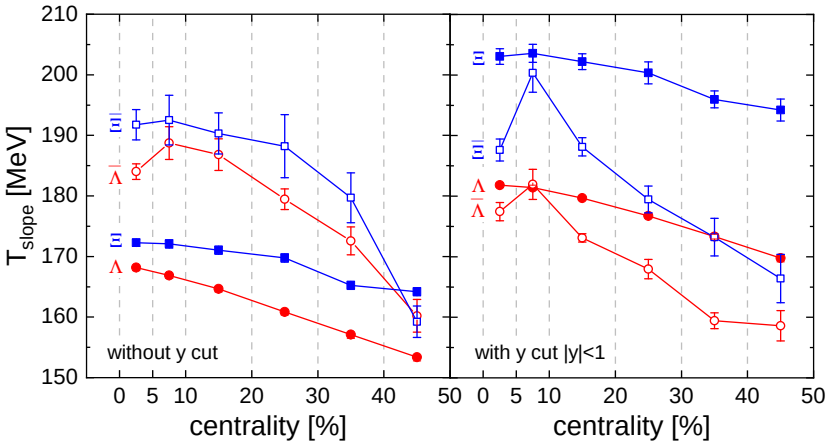


Figure 7. Slope parameters of transverse momentum distributions of Λ, Ξ, $\overline{\Lambda}$, and $\overline{\Xi}$ hyperons within the momentum interval $0.5 \leq p_T \leq 1.5$ GeV for different centrality bins without any cuts (**left panel**), and for the rapidity cut $|y| < 1$ (**right panel**). If error bars are not visible, they are smaller than the symbol size.

Both the slope of p_T spectra and the width of rapidity spectra suggest that observed anti-hyperons decouple from the fireball mainly at earlier stages of its evolutions than hyperons. This agrees with the analysis of Au + Au collisions [26,27], where we argued that this explains the larger magnitude of the global spin polarization of anti-hyperons.

3. Vorticity Field and Spin Polarization

For the calculations of the hyperon spin polarization, we use the thermodynamic approach [9,61], where the local spin polarization of a particle with mass m and spin s is induced by the local thermal vorticity,

$$\varpi_{\mu\nu} = \frac{1}{2}\left[\partial_\nu\left(\frac{u_\mu}{T}\right) - \partial_\mu\left(\frac{u_\nu}{T}\right)\right] = \frac{\omega_{\mu\nu}}{2T} - \frac{1}{2T}\Big[u_\mu\partial_\nu \ln T - u_\nu\partial_\mu \ln T\Big], \tag{11}$$

where u_ν is the hydrodynamic 4-velocity of a fluid element and T is its temperature. In the second equation, here we separated the kinematic vorticity $\omega_{\mu\nu} = (\partial_\nu u_\mu - \partial_\mu u_\nu)$. The latter tensor provides a natural relativistic generalization for the non-relativistic vorticity, $\boldsymbol{\omega} = \mathrm{rot}\,\boldsymbol{u}$: $\omega_{\mu\nu} = -\epsilon_{\mu\nu\rho\sigma}u^\rho\bar{\omega}^\sigma$. The components of the relativistic vorticity vector are $\bar{\omega}^\mu = \gamma^2\big((\boldsymbol{u}\boldsymbol{\omega}), \boldsymbol{\omega} + [\boldsymbol{u}\times\partial_t\boldsymbol{u}]\big)$. Then, hyperons with spin s, momentum p_μ and mass m_H contained in this fluid element will have average spin described by the 4-vector,

$$S^\mu(x,p) = -\frac{s\,(s+1)}{6\,m_H}(1-n(x,p))\varepsilon^{\mu\nu\lambda\delta}\varpi_{\nu\lambda}p_\delta, \tag{12}$$

to the leading order in the vorticity $\varpi_{\mu\nu}$. Here, $n(x,p)$ is the hyperon distribution function. Applying Relation (12), we do not assume that the system has reached global thermal equilibrium. We determine local thermodynamic parameters of the medium, like temperature and density performing ensemble averaging over many collision events. Particularly, to determine the fluid velocity, $\boldsymbol{u}$, and the energy density, ε, we calculate averaged energy–momentum tensor for the particle distribution generated by the PHSD code, and find its eigenvectors $\boldsymbol{u}$ and eigenvalues ε at any moment of the system evolution. The applied procedure is described in detail in Ref. [34]. We have to emphasize that we do not solve hydrodynamic equations as, for instance, in the hybrid approaches like SMASH

and UrQMD, and the evolution of the velocity, density, and density fields follows from the microscopic transport calculations, see also Ref. [62]. Given local vorticity field $\varpi(x)$, we can estimate the averaged spin polarization of the fermion created at this point; for details, see Ref. [27].

Distinguishing features of our approach are, first, the clear separation of nucleon-spectators and nucleon-participants. Only the latter ones contribute their angular momentum to the system leading to the vorticity creation. Second, only the fluid cells with the energy density $> 0.05\,\mathrm{GeV/fm^3}$ are taken into account in the vorticity calculations. By this, we eliminate cells with an on-average small number of particles in every collision event to get rid of the areas far from hydrodynamic regime and exclude thereby high fluctuating gradients due to extremely small densities and temperatures.

The obtained range of temperatures and densities is such that hyperon momentum distributions are essentially non-degenerate and, therefore, we can work in the Boltzmann limit by putting $(1 - n(x,p)) \approx 1$ into Equation (12).

The velocity and vector fields created in the Bi + Bi collision at $\sqrt{s_{NN}} = 9.0\,\mathrm{GeV}$ are found to be qualitatively very similar to those for Au + Au collision at $\sqrt{s_{NN}} = 7.7\,\mathrm{GeV}$, which we studied in detail in Refs. [26,34]. Therefore, we only briefly discuss here the general structure of the fields that are relevant for the further discussion of the angular dependence of the hyperon polarization. The evolution of the velocity field in Bi + Bi collision at the selected value of the impact parameter $b = 8.5\,\mathrm{fm}$ that corresponds to the centrality class 30–40% (see Figure 1) is shown in Figure 8 for three time moments. As was shown in Ref. [34], the velocity field consists mainly of the Hubble-like component, which can be written in the cylindrical coordinate system (r_T, ϕ, z) as

$$\boldsymbol{u}_{\mathrm{H}} = \alpha_T\, r_T^{\beta_T}\, \boldsymbol{e}_T + \alpha_{\parallel}\, z^{\beta_{\parallel}}\, \boldsymbol{e}_z\,, \tag{13}$$

where coefficients α_T, β_T and $\alpha_{\parallel}$, $\beta_{\parallel}$ do not depend on coordinates (but may change with time) and $\boldsymbol{e}_T = (\cos\phi, \sin\phi, 0)$ and $\boldsymbol{e}_z = (0,0,1)$ are the unit vectors in the transverse and longitudinal directions. The evolution of transverse and longitudinal components of the velocity are presented in Figures 9 and 10 in Ref. [34].

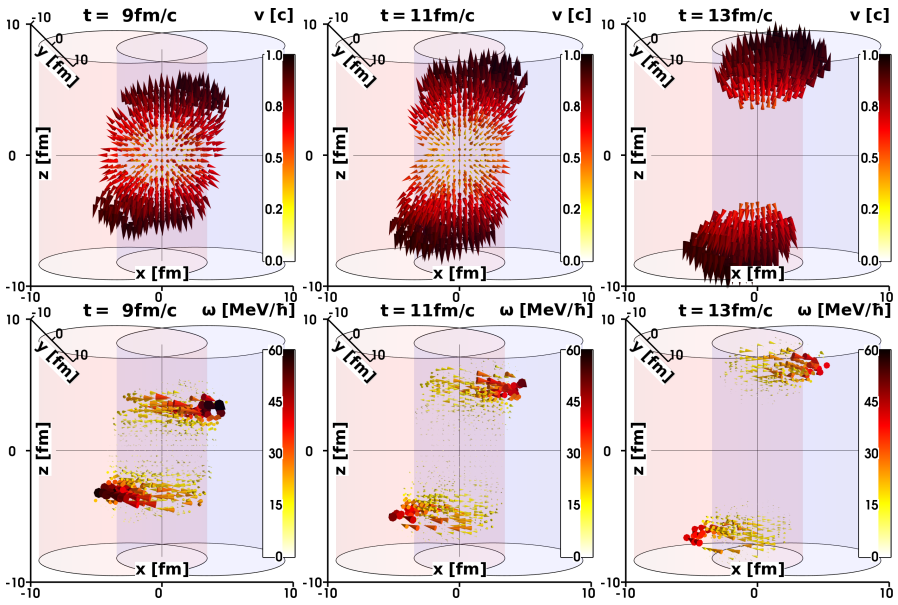


Figure 8. Hydrodynamic velocity, $\boldsymbol{u}$, (**upper row**) and corresponding vorticity, $\boldsymbol{\omega} = \mathrm{rot}\,\boldsymbol{u}$, (**lower row**) fields created in Bi + Bi collision at the collision energy $\sqrt{s_{NN}} = 9.0\,\mathrm{GeV}$ and the impact parameter $b = 8.5\,\mathrm{fm}$ at three moments of time. The moment of the full overlap of colliding nuclei corresponds to $\simeq$5.5 fm/c. Two overlapping cylinders indicate trajectories of colliding nuclei. The y axis points away from the reader so that the x, y, z axes form the right-handed coordinate system.

The Hubble-like component is irrotational, i.e., $\mathrm{rot}\,\boldsymbol{u}_{\mathrm{H}} = 0$. The strict mathematical Stokes–Helmholtz decomposition of a vector field in irrotational and solenoidal parts is rather computationally involved and is, actually, not necessary for the study of spin polarization. We discussed some approximate methods of separation of the Hubble-like component in Ref. [63]. The analysis in [34] of the velocity fields generated with the fluidized PHSD model shows that, on average, the correction terms are numerically much smaller than the Hubble-like term: $|\boldsymbol{u} - \boldsymbol{u}_{\mathrm{H}}| \ll \boldsymbol{u}_{\mathrm{H}}$. We also find the same for the Bi + Bi collisions. There are several sources for a small admixture of a vortical component, $\boldsymbol{u}_\omega$, i.e., $\mathrm{rot}\,\boldsymbol{u}_\omega = \boldsymbol{\omega} \neq 0$, which we discuss qualitatively in order to justify the observed structure of the vorticity field. A contribution to the vorticity occurs if the coefficient α_T and $\alpha_\parallel$ in (13) acquire a residual dependence on z and r_T, respectively, than $\mathrm{rot}\,\boldsymbol{u}_H = -\big(z\partial_{r_T}\alpha_\parallel - r_T\partial_z\alpha_T\big)\boldsymbol{e}_\phi$. We see that it creates a circular vorticity field. Another contribution is due to the term violating the axial symmetry and corresponding to a time and z-coordinate shift of the center of the transverse Hubble-like expansion, $(x_0, 0)$: $\delta\boldsymbol{u}_{\mathrm{asym}} = -\alpha_T x_0(z,t)\Big(\cos\phi\boldsymbol{e}_T - \sin\phi\boldsymbol{e}_\phi\Big)$, where $\boldsymbol{e}_\phi$ is the azimuthal unit vector $\boldsymbol{e}_\phi = [\boldsymbol{e}_z \times \boldsymbol{e}_T] = (-\sin\phi, \cos\phi, 0)$. The shift of the center of the transverse expansion is visible in the upper row in Figure 8. Such a tilt in the particle emission source with respect to collision axis could be tested, e.g., by the two-pion momentum correlations; see [64,65]. Contribution $\delta\boldsymbol{u}_{\mathrm{asym}}$ to the fluid velocity produces the axially asymmetric vorticity field $\mathrm{rot}\,\delta\boldsymbol{u}_{\mathrm{asym}} = -\alpha_T\partial_z x_0(z,t)\big(\sin\phi\boldsymbol{e}_T + \cos\phi\boldsymbol{e}_\phi\big) = -\alpha_T\partial_z x_0(z,t)(1,0,0)$. Both of the above effects lead to the formation of an asymmetric vortex ring, which has a form of a bublik (an asymmetric donut), see detailed investigation in [34]. The formation of vortex rings was also proposed in Ref. [66]. The vorticity field generated by the PHSD model is shown in Figure 8, and clearly demonstrates two bubliks moving in the opposite direction along the z axis and having the opposite direction of vorticities. The bubliks are slowly expanding in the transverse direction. The details on the structure of the vorticity field and its evolution can be seen in Figure 13 of Ref. [34]. For the Bi + Bi collisions at the energies considered in this paper, the maximum magnitude of the kinematic vorticity over the fireball grows, first from the time of the full nucleus overlap ($t \sim 5\,\mathrm{fm}/c$) to $t \sim 7\,\mathrm{fm}/c$ between $\omega \simeq 70\,\mathrm{MeV}/\hbar$ and $80\,\mathrm{MeV}/\hbar$. Then, it gradually decreases down to $\simeq$40 MeV at $t \sim 13\,\mathrm{fm}/c$.

In Figure 8, we can note that the maximum of the vorticity magnitude is located at the border of the intersection of colliding nuclei. This can be understood if we recall the equation for the vorticity dynamics, which follows from the Navier–Stokes equation [67] (see also Ref. [34]),

$$\frac{\partial\boldsymbol{\omega}}{\partial t} + [\boldsymbol{\nabla} \times [\boldsymbol{\omega} \times \boldsymbol{v}]] = \nu\Delta\boldsymbol{\omega} + \frac{1}{\rho^2}[\boldsymbol{\nabla}\rho \times \boldsymbol{\nabla}p]\,, \tag{14}$$

where the first term on the right-hand side with the kinematic shear viscosity, ν, is responsible for the decay of the vorticity due to diffusion. The second term is the vorticity source term. This term is called the Biermann battery following Ref. [68], where a similar term was considered as a source of the magnetic field in stars. The source term is non-zero when the pressure is nonbarotropic, i.e., depends not only on the particle density, but also on the temperature (or entropy) of the system, as it is for the nuclear equation of state. Thus, the vorticity is generated when a density gradient is not collinear with a temperature gradient, $[\nabla\rho \times \nabla p] \propto [\nabla\rho \times \nabla T] \neq 0$. This occurs at the initial stage of the fireball formation, when colliding nuclei are interpenetrating at the border of their contact.

Within our dynamical freeze-out approach, at each time step, if a particle occurs inside the medium as a result of a non-decay process like particle creation or rescattering, then the particle's spin vector is calculated according to Equation (12). Recall that, under the medium we understand only the fluid elements with the energy density $\varepsilon > 0.05\,\mathrm{GeV}/\mathrm{fm}^3$.

The hyperon polarization $\boldsymbol{P} = \boldsymbol{S}^*/s$ is then determined by the spin vector recalculated in the rest frame of the hyperon,

$$\boldsymbol{S}^* = \boldsymbol{S} - \frac{(\boldsymbol{Sp})\,\boldsymbol{p}}{E(E+m)}, \tag{15}$$

where we used $S_0 E = (\boldsymbol{Sp})$, since $S^\mu p_\mu \equiv 0$. If a particle ends up outside the medium, the particle polarization is set to zero. This means that such particles will not contribute to the accumulated spin of hyperons.

In the PHSD model, strong hyperon decays are dynamically included in the evolution of the system. For strong decays $\Sigma^* \to \Lambda + \pi$ and $\Xi^* \to \Xi + \pi$, the polarization of the initial hyperon is in part transferred to the daughter hyperon, according to the relations derived in Ref. [11]; see Section 4 of Ref. [26] for details. They are based on the consideration that the momentum-independent mean polarization of the daughter fermion is proportional to that of the parent one, and a dynamical matrix independent coefficient can be used; see Equation (37) and Table 1 in Ref. [11] and appendices there. Finally, hyperons that survive until the full dissolution of the medium will carry information about the medium and polarization at the time of their last interaction; see Ref. [26] for details.

Applying this algorithm to Λ or $\overline{\Lambda}$ hyperons, and averaging over all generated collision events, we can determine the averaged global polarizations of hyperon as the y projection of the vector,

$$\langle \boldsymbol{P}_H \rangle = 2\,\langle \boldsymbol{S^*}_H \rangle. \tag{16}$$

The y axis is always normal to the reaction plane in our simulations. This is primary and not yet a final observable polarization signal, since the weak and electromagnetic decays, $\Xi \to \Lambda + \pi$ and $\Sigma^0 \to \Lambda + \gamma$, are not yet taken into account.

In Figure 9, we present polarization maps of the transverse momentum p_T and rapidity y for the minimum bias Bi + Bi collisions. One can see a plateau of positive polarization in the $|y| \lesssim 1.5$ and $p_T \lesssim 1.5\,\mathrm{GeV}/c$ area for hyperons and $|y| \lesssim 1$ and $p_T \lesssim 1\,\mathrm{GeV}/c$ for anti-hyperons. Peripheral zones of rapidity and transverse momentum have large fluctuations of polarization in the neighboring cells. There are very few particles in this cells and the energy density is below the threshold value $0.05\,\mathrm{GeV/fm^3}$. Therefore, hyperons occurring in these cells acquire the zero polarization. With a further increase in the number of collision events, the contributions from these zones to the total polarization average to zero. By using such maps separated for different centrality classes, we can study the influence of experimental cuts on the observable polarization signal.

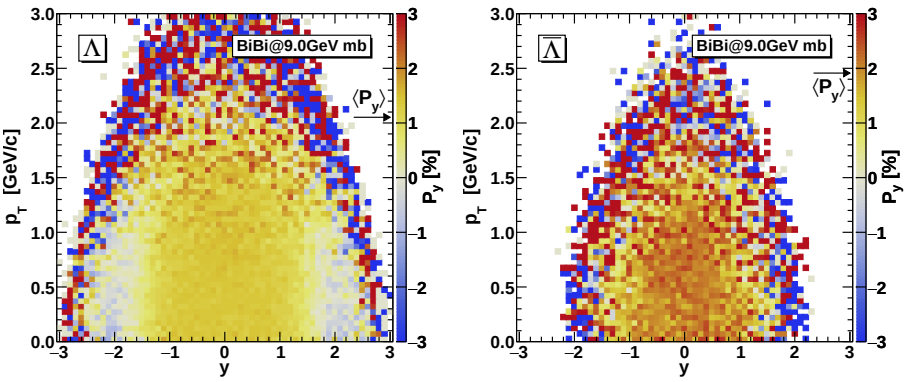


Figure 9. The spin polarization distributions as functions of p_T and y for Λ (**left panel**) and $\overline{\Lambda}$ (**right panel**) hyperons for the minimum bias Bi + Bi collisions at $\sqrt{s_{NN}} = 9.0\,\mathrm{GeV}$. The average polarizations for these distributions are shown by arrows on the scale.

The polarization maps, as shown in Figure 9, can be prepared including only the events of a certain centrality class. Then, vertically summing up the p_T bins, we obtain the rapidity distributions of the polarization for different centrality classes that are shown in Figure 10. For centrality classes $< 30\%$, the polarization weakly depends on rapidity

if $|y| < 1$ and increases if $|y| < 0.5$ for classes 30–40% and 40–50%. This dependence is stronger for $\overline{\Lambda}$. We observe also that the p_T cut has a weak influence on the rapidity dependence of the spin polarization.

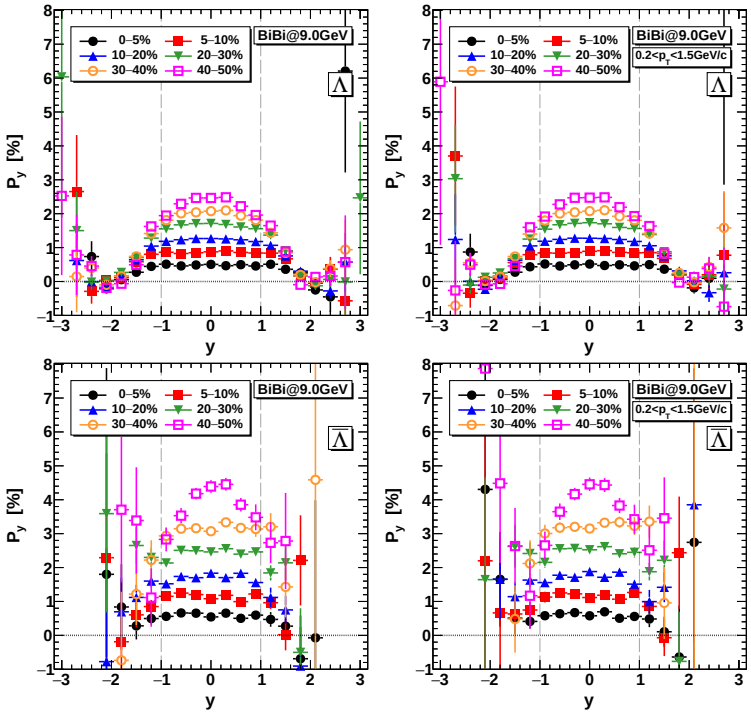


Figure 10. The spin polarizations of Λ (**upper row**) and $\overline{\Lambda}$ (**lower row**) hyperons as functions of the rapidity without momentum cuts (**left panels**) and with the transverse momentum cut $0.2 < p_T < 1.5\,\mathrm{GeV}/c$ (**right panels**).

In Figure 11, we show the results of the summation of the rapidity bins in Figure 9 with the selection of different centrality classes. We see that the spin polarization signal for Λs almost does not change within the $0.2 < p_T < 1.5\,\mathrm{GeV}$ window. For $p_T > 1.5\,\mathrm{GeV}$, the polarization fluctuations increase significantly. For $\overline{\Lambda}$, the polarization varies with stronger p_T, and for $p_T > 1.5\,\mathrm{GeV}$, statistical errors become very large. Comparing the left and right panels, we conclude that the influence of rapidity cut is rather small.

Similar y and p_T dependence of the polarization is found for Σ, Ξ, and Ω hyperons and the corresponding anti-particles.

We turn now to the question of how the global spin polarization of various hyperon species changes with centrality. It is shown in Figure 12 without (left panel) and with acceptance constraints (right panel). As seen, the polarization of all hyperons increases with a centrality class increase from the most central collision until the centrality class ∼60–70%. Then, it starts decreasing. At the maximum, the Ω hyperons are most polarized in the case without rapidity and p_T cuts. With the cuts, Λs and Ωs are similarly polarized. Polarization of all anti-hyperons are alike and maximal in the same centrality class as hyperons. We see also that the polarization magnitude for anti-hyperons is approximately twice larger than that for hyperons. The acceptance cut almost does not affect the anti-hyperons, but significantly increases the resulting polarization for hyperons, especially for peripheral collisions.

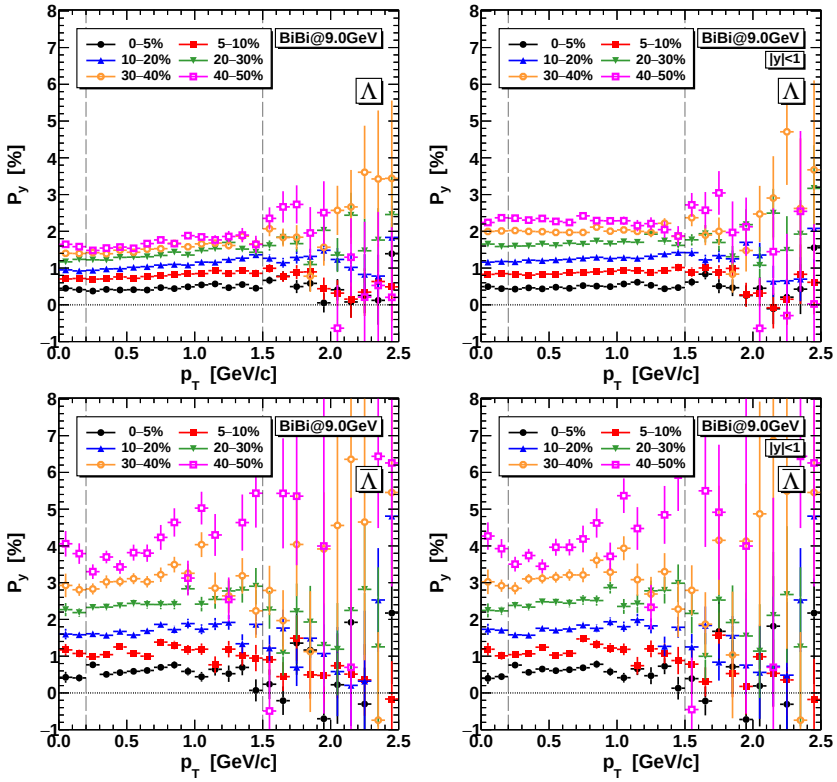


Figure 11. The spin polarizations of Λ (**upper row**) and $\overline{\Lambda}$ (**lower row**) hyperons as functions of the transverse momentum without the rapidity cut (**left panels**) and with the rapidity cut $|y| < 1$ (**right panels**).

As mentioned above, only strong decays of hyperon resonances are taken into account in the PHSD transport model. When all strong interactions stop, the family of Λ hyperons is additionally populated due to weak and electromagnetic decays $\Xi \to \Lambda + \pi$ and $\Sigma^0 \to \Lambda + \gamma$. The polarization transfer in these reactions is taken into account applying the relations from Refs. [11,20]. In the same way, the feed-down corrections are applied for $\overline{\Lambda}$s; see Refs. [26,27]. The Λ and $\overline{\Lambda}$ polarizations including the feed-down effects are shown in Figure 12. We observe a suppression of the Λ and $\overline{\Lambda}$ polarizations (up to $\approx$36%); compare the red and black symbols. The main role, thereby, is played by the decays of $\Sigma^0(\overline{\Sigma}^0)$ hyperons because of their large relative abundance. Nevertheless, our calculations [26] reproduce the polarization signals for both Λ and $\overline{\Lambda}$ at higher collision energy $\sqrt{s_{NN}} = 11.5$ GeV. The Λ polarization for $\sqrt{s_{NN}} = 7.7$ GeV is also well described; however, the $\overline{\Lambda}$ polarization is underestimated. The $\Xi(\overline{\Xi})$ and $\Omega(\overline{\Omega})$ polarizations do not suffer from the feed-down effect.

The experimental feasibility of polarization signal registration depends on the particle abundance [30]. The magnitude of the polarization signal is compared with the number of produced hyperons for different centrality classes in Table 1. The largest number of particles can be registered for the broadest centrality classes 10–50% and 10–60%. Narrowing the centrality window towards the less-central collision gives a larger global spin polarization, e.g., 2.37% for primary Λs and 4.22% for primary $\overline{\Lambda}$s, but the number of produced hyperons decreases by a factor of $\sim$3. The account for the hyperon feed-down increases the number of Λs by a factor of 1.5 and the $\overline{\Lambda}$ number by a factor of $\sim$2. At the same time, the global spin polarization falls down equally for Λs and $\overline{\Lambda}$s by a factor of $\sim$1.5.

Using Table 1, we may conclude that is more feasible to measure the polarization signal in semi-central collisions or in broad centrality bins. For example, considering the 50–70% centrality bin instead of the 10–50% bin, we may increase polarization signals for Λs by 60% and for $\overline{\Lambda}$ by a factor of 2, but the number of particles drops by a factor of $\sim$4 for Λs and by a factor of $\sim$6 for $\overline{\Lambda}$s.

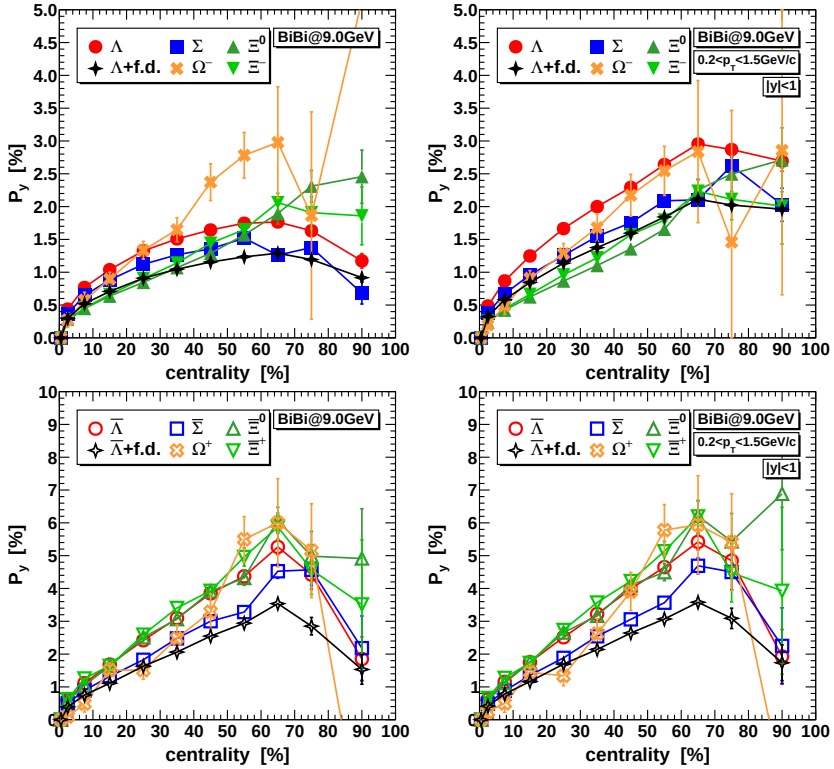


Figure 12. The dependence of the global spin polarization for various hyperons (**upper row**) and anti-hyperons (**lower row**) on the collision centrality for Bi + Bi collisions at $\sqrt{s_{NN}} = 9.0\,\mathrm{GeV}$ without momentum cuts (**left panels**) and for the midrapidity region $|y| < 1$ with the transverse momentum cut $0.2 < p_T < 1.5\,\mathrm{GeV}/c$ (**right panels**).

Table 1. The global spin polarizations and multiplicities of the Λ and $\overline{\Lambda}$ hyperons in Bi + Bi collisions at $\sqrt{s_{NN}} = 9.0\,\mathrm{GeV}$ for the rapidity range $|y| < 1$ and the transverse momentum range $0.2\,\mathrm{GeV}/c < p_T < 1.5\,\mathrm{GeV}/c$ depending on the different centrality classes. Numbers in brackets indicate statistical errors.

	Λ(prim.)		**Λ**		**$\overline{\Lambda}$(prim.)**		**$\overline{\Lambda}$**	
Centrality	***N***	***P_y*, %**	***N***	***P_y*, %**	***N***	***P_y*, %**	***N***	***P_y*, %**
10–50%	11.97 (2)	1.60 (1)	17.61 (2)	1.09 (1)	0.25 (1)	2.43 (2)	0.48 (1)	1.62 (1)
10–60%	10.28 (2)	1.67 (1)	15.10 (2)	1.14 (1)	0.21 (1)	2.55 (2)	0.40 (1)	1.70 (1)
10–70%	8.93 (2)	1.71 (1)	13.10 (2)	1.17 (1)	0.18 (1)	2.61 (2)	0.34 (1)	1.74 (1)
20–50%	9.47 (1)	1.86 (1)	13.84 (2)	1.28 (1)	0.19 (1)	2.98 (3)	0.35 (1)	1.99 (2)
20–60%	7.99 (1)	1.94 (1)	11.64 (2)	1.34 (1)	0.15 (1)	3.13 (3)	0.29 (1)	2.08 (2)
20–70%	6.83 (1)	1.99 (1)	9.93 (2)	1.37 (1)	0.13 (1)	3.21 (3)	0.24 (1)	2.14 (2)
30–50%	7.80 (1)	2.08 (1)	11.33 (1)	1.43 (1)	0.14 (1)	3.50 (5)	0.27 (1)	2.32 (3)
30–60%	6.38 (1)	2.17 (1)	9.24 (1)	1.50 (1)	0.11 (1)	3.70 (5)	0.21 (1)	2.44 (3)
30–70%	5.33 (1)	2.23 (1)	7.71 (1)	1.55 (1)	0.09 (1)	3.81 (5)	0.17 (1)	2.52 (3)
40–50%	6.27 (1)	2.25 (2)	9.06 (1)	1.56 (1)	0.11 (1)	3.99 (9)	0.20 (1)	2.63 (6)
40–60%	4.90 (1)	2.37 (2)	7.06 (1)	1.65 (1)	0.08 (1)	4.22 (8)	0.15 (1)	2.78 (5)
40–70%	4.00 (1)	2.45 (2)	5.74 (1)	1.71 (1)	0.06 (1)	4.35 (8)	0.12 (1)	2.87 (5)
50–70%	2.86 (1)	2.66 (3)	4.08 (1)	1.87 (2)	0.04 (1)	4.80 (13)	0.08 (1)	3.17 (8)
50–100%	1.54 (1)	2.67 (3)	2.18 (1)	1.89 (2)	0.02 (1)	4.60 (13)	0.04 (1)	3.06 (8)
60–100%	1.04 (1)	2.79 (5)	1.46 (1)	2.00 (3)	0.01 (1)	4.57 (24)	0.02 (1)	3.09 (15)
70–100%	0.66 (1)	2.71 (8)	0.91 (1)	1.94 (6)	0.01 (1)	3.72 (44)	0.01 (1)	2.55 (27)

4. Angular Dependence of the Spin Polarization

Several sources of the spin polarization in heavy-ion collisions are considered in the literature. Some of them are related to the vorticity of the medium [9], others to the

formation of helicity field, $h = (\omega v)$, [69,70]. It is interesting whether experimental data could reveal information about an operative polarizing mechanism. In Ref. [34], we argue that the helicity field created in HICs has a prominent plane symmetry: on one side of the reaction plane, the helicity is positive and is negative on the other side. Also, we demonstrated that, by selecting hyperons with a positive or negative projection of the hyperon momentum on the axis perpendicular to the reaction plane, one can probe regions with different helicities. The mechanism of the spin polarization, which we consider here, is due to the vorticity field. Our calculations show that the latter has a peculiar structure of two asymmetrical rings (bubliks) moving in opposite directions; see Figure 8. One can try to separate the hyperons stemming from the most vortical parts of the bubliks. They would have opposite polarization directions, P_y. For this, we select positive or negative projections of the momenta along the collision axis, $p_z \gtrless 0$, and look at the dependence of the hyperon polarization on the azimuthal angle, $\cos\phi_H = p_x/p_T$. The spin polarization as a function of $\cos\phi_H$ is shown in Figure 13 for $p_z > 0$ and $p_z < 0$. We observe a drastically different behavior of the $P_y(\cos\phi_H)$ function: it is rising for $p_z > 0$ and decreasing for $p_z < 0$. It can be parameterized as

$$\langle P_{y,H} \rangle \propto (1 + \beta_{H,1}(p_z)\cos\phi_H + \beta_{H,2}(p_z)\cos^2\phi_H), \quad H = \Lambda,\ \Xi,\ \overline{\Lambda},\ \overline{\Xi}, \tag{17}$$

where the coefficient $\beta_{H,1}(p_z)$ is approximately anti-symmetrical function of p_z, and $\beta_{H,2}(p_z)$ is approximately symmetrical one. For the given statistics, $|\beta_{2,H}|$ is much smaller than $|\beta_{1,H}|$ for hyperons Λ and Ξ but for anti-hyperons $\overline{\Lambda}$ and $\overline{\Xi}$ its contribution is visible; see plots in lower panels of Figure 13 and in the right panel of Figure 14. For primary Λs and $\overline{\Lambda}$s without the electromagnetic and weak feed-down the angular dependence of the polarization signal is more pronounced, as seen in the left panels of Figure 13.

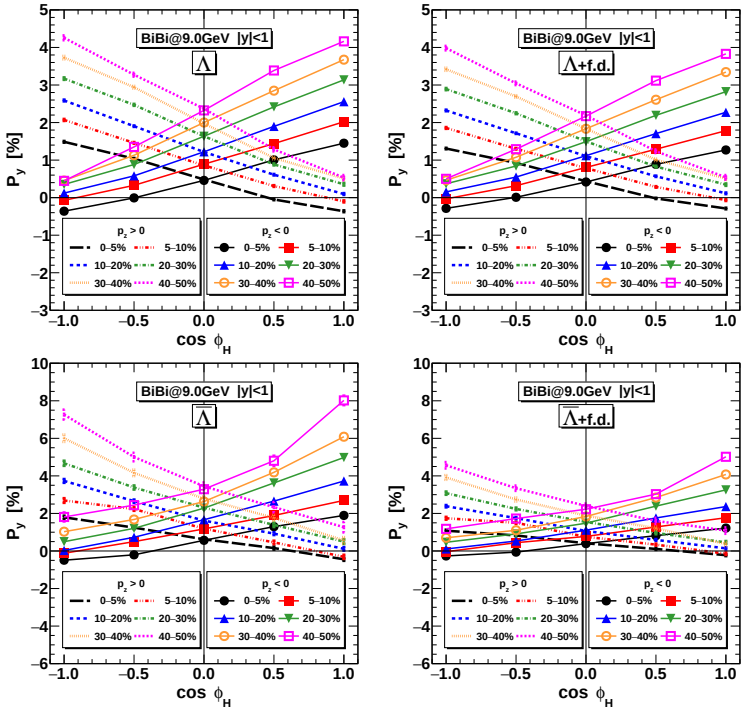


Figure 13. The spin polarizations of Λ (**upper row**) and $\overline{\Lambda}$ (**lower row**) hyperons as functions of the azimuthal angle in the transverse momentum plane for various centrality classes without feed-down due to electromagnetic and weak decays (**left panels**) and with it (**right panels**).

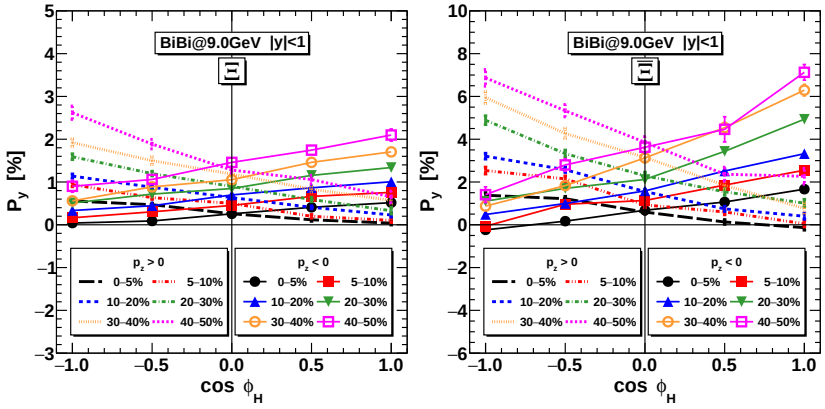


Figure 14. The spin polarizations of Ξ (**left panel**) and $\overline{\Xi}$ (**right panel**) hyperons as functions of the azimuthal angle in the transverse momentum plane for various centrality classes.

The experimental observation of such patterns would speak for the vortical mechanism of polarization and the particular structure of the vorticity field.

5. Conclusions

The hyperon production in collisions of two bismuth nuclei at energy $\sqrt{s_{NN}} = 9.0$ GeV is studied within the PHSD transport model. Yields of strange particles, Λ, Σ, Ξ, and Ω, and the corresponding anti-particles, are calculated for various centrality classes. The hierarchy of Λ, Ξ, and Ω yields for the most central collisions is found to be similar to the hierarchy observed in central Pb + Pb collisions at $\sqrt{s_{NN}} = 8.77$ GeV by the NA49 collaboration. Also, the hierarchy of measured anti-particles $\overline{\Lambda}$ and $\overline{\Xi}$ is alike the experimental one. The influence of the transverse momentum, p_T, and rapidity cut, y, is investigated. The hyperon yields demonstrate the stronger dependence on the rapidity cut than on the p_T cuts. The rapidity spectra of Λ and Ξ hyperons and corresponding anti-particles are calculated and analyzed. The y distributions for anti-hyperons are found to be more compact than those of hyperons. The slope parameters of the p_T spectrum for Λ and Ξ show a weak variation with the collision centrality which, however, is significantly stronger for $\overline{\Lambda}$ and $\overline{\Xi}$. Restricting the rapidity range leads to a significant increase in the slope parameter: by ∼15 MeV for Λs and by ∼30 MeV for Ξs. Changes in the slopes for anti-hyperons are less significant.

We performed fluidization of the particle distributions generated by the PHSD transport code and determined evolutions of the velocity and vorticity fields, assuming that the velocity is defined within the Landau frame. Vorticity is shown to be concentrated in the form of two asymmetrical vortex rings moving in opposite directions. Averaged spin polarizations of hyperons and anti-hyperons induced by the local thermal vorticity are evaluated. We analyzed the dependence of the polarization signal on the collision centrality and momentum cuts. For anti-hyperons, the p_T and rapidity cuts do not change the polarization signal for centralities <40%. However, the cuts affect the polarizations of hyperons. The polarization signal is almost linearly rising with the centrality (from central to peripheral collisions) exhibiting a maximum for the 60–70% centrality class. The final polarization of Λ and $\overline{\Lambda}$ particles are calculated with the account for feed-down effects due to the weak, $\Xi \to \Lambda + \pi$, and electromagnetic, $\Sigma^0 \to \Lambda + \pi^0$, decays. The feed-down increases the number of final Λs by a factor of 1.5 and $\overline{\Lambda}$ by a factor of 2. The polarization signal decreases equally for Λs and $\overline{\Lambda}$s by a factor of ∼1.5. We showed that the vortical mechanism of the spin polarization and the particular structure of the vorticity field manifest themselves through the dependence of the polarization signal on the azimuthal angle of the outgoing hyperon. Thereby, the polarization increases for particles with $p_z > 0$ and decreases for $p_z < 0$; see Figure 13. Also, for Λ hyperons, the dependence is almost linear, whereas for $\overline{\Lambda}$ there is a small admixture of a quadratic component. For primary Λ and $\overline{\Lambda}$ hyperons the angular dependence is more pronounced. A similar pattern is found also for the Ξ and $\overline{\Xi}$ hyperons as shown in Figure 14. Thus, we conclude that the experimental

study of the angular dependence of the polarization signal in the transverse plane could reveal information about possible polarization mechanisms.

Author Contributions: All authors have equally contributed to conceptualization, validation, writing and editing of the draft. All authors have read and agreed to the published version of the manuscript.

Funding: This research was partially supported by the Slovak grant VEGA 1/0521/22. The calculations were performed on the "Govorun" computational cluster provided by the Laboratory of Information Technologies of JINR, Dubna.

Institutional Review Board Statement: Not applicable.

Informed Consent Statement: Not applicable.

Data Availability Statement: Data are contained within the article.

Acknowledgments: We thank D.N. Voskresensky, Yu.B. Ivanov and A.V. Taranenko for discussions.

Conflicts of Interest: The authors declare no conflicts of interest.

Abbreviations

The following abbreviations are used in this manuscript:

AGS	Alternating Gradient Synchrotron
BM@N	Baryonic Matter at Nuclotron
EoS	Equation of State
HADES	High Acceptance Di-Electron Spectrometer
HIC	Heavy-Ion Collision
LHC	Large Hadron Collider
MPD	Multi-Purpose Detector
NICA	Nuclotron-based Ion Collider Facility
PHSD	Parton Hadron String Dynamics
QGP	Quark-Gluon Plasma
QGSM	Quark-Gluon String Model
RHIC	Relativistic Heavy Ion Collider
SIS	Schwer-Ionen-Synchrotron (heavy-ion synchrotron)
SPS	Super Proton Synchrotron
STAR	Solenoidal Tracker at RHIC
UrQMD	Ultra-relativistic Quantum Molecular Dynamics

References

1. Acharya, S.; Adamová, D.; Adhya, S.P.; Adler, A.; Adolfsson, J.; Aggarwal, M.M.; Aglieri Rinella, G.; Agnello, M.; Agrawal, N.; Ahammed, Z.; et al. Global polarization of Λ and $\overline{\Lambda}$ hyperons in Pb-Pb collisions at $\sqrt{s_{NN}} = 2.76$ and 5.02 TeV. *Phys. Rev. C* **2020**, *101*, 044611. [CrossRef]
2. Abou Yassine, R.; Adamczewski-Musch, J.; Asal, C.; Becker, M.; Belounnas, A.; Blanco, A.; Blume, C.; Chlad, L.; Chudoba, P.; Ciepał, I.; et al. Measurement of global polarization of Λ hyperons in few-GeV heavy-ion collisions. *Phys. Lett. B* **2022**, *835*, 137506. [CrossRef]
3. Adamczyk, L.; Adkins, J.K.; Agakishiev, G.; Aggarwal, M.M.; Ahammed, Z.; Ajitanand, N.N.; Alekseev, I.; Anderson, D.M.; Aoyama, R.; Aparin, A.; et al. Global Λ hyperon polarization in nuclear collisions: Evidence for the most vortical fluid. *Nature* **2017**, *548*, 62–65. [CrossRef]
4. Félix, J. On theoretical studies of Λ^0 polarization. *Mod. Phys. Lett. A* **1999**, *14*, 827. [CrossRef]
5. Liang, Z.T.; Wang, X.N. Globally polarized quark-gluon plasma in noncentral $A + A$ collisions. *Phys. Rev. Lett.* **2005**, *94*, 102301. [CrossRef]
6. Ladygin, V.P.; Jerusalimov, A.P.; Ladygina, N.B. Polarization of Λ^0 hyperons in nucleus-nucleus collisions at high energies. *Phys. Part. Nucl. Lett.* **2010**, *7*, 349. [CrossRef]
7. Becattini, F.; Lisa, M.A. Polarization and vorticity in the quark–gluon plasma. *Ann. Rev. Nucl. Part. Sci.* **2020**, *70*, 395–423. [CrossRef]
8. Becattini, F.; Tinti, L. The ideal relativistic rotating gas as a perfect fluid with spin. *Ann. Phys.* **2010**, *325*, 1566–1594. [CrossRef]
9. Becattini, F.; Chandra, V.; Del Zanna, L.; Grossi, E. Relativistic distribution function for particles with spin at local thermodynamical equilibrium. *Ann. Phys.* **2013**, *338*, 32–49. [CrossRef]

10. Fang, R.H.; Pang, L.G.; Wang, Q.; Wang, X.N. Polarization of massive fermions in a vortical fluid. *Phys. Rev. C* **2016**, *94*, 024904. [CrossRef]
11. Becattini, F.; Karpenko, I.; Lisa, M.A.; Upsal, I.; Voloshin, S.A. Global hyperon polarization at local thermodynamic equilibrium with vorticity, magnetic field, and feed-down. *Phys. Rev. C* **2017**, *95*, 054902. [CrossRef]
12. Karpenko, I.; Becattini, F. Study of Λ polarization in relativistic nuclear collisions at $\sqrt{s_{\rm NN}}$ = 7.7–200 GeV. *Eur. Phys. J. C* **2017**, *77*, 213. [CrossRef]
13. Xie, Y.; Wang, D.; Csernai, L.P. Global Λ polarization in high energy collisions. *Phys. Rev. C* **2017**, *95*, 031901. [CrossRef]
14. Ivanov, Y.B.; Toneev, V.D.; Soldatov, A.A. Estimates of hyperon polarization in heavy-ion collisions at collision energies $\sqrt{s_{NN}} = 4 - 40$ GeV. *Phys. Rev. C* **2019**, *100*, 014908. [CrossRef]
15. Ivanov, Y.B.; Soldatov, A.A. Correlation between global polarization, angular momentum, and flow in heavy-ion collisions. *Phys. Rev. C* **2020**, *102*, 024916. [CrossRef]
16. Ivanov, Y.B. Global Λ polarization in moderately relativistic nuclear collisions. *Phys. Rev. C* **2021**, *103*, L031903. [CrossRef]
17. Ivanov, Y.B.; Soldatov, A.A. Global Λ polarization in heavy-ion collisions at energies 2.4–7.7 GeV: Effect of meson-field interaction. *Phys. Rev. C* **2022**, *105*, 034915. [CrossRef]
18. Li, H.; Pang, L.G.; Wang, Q.; Xia, X.L. Global Λ polarization in heavy-ion collisions from a transport model. *Phys. Rev. C* **2017**, *96*, 054908. [CrossRef]
19. Sun, Y.; Ko, C.M. Λ hyperon polarization in relativistic heavy ion collisions from a chiral kinetic approach. *Phys. Rev. C* **2017**, *96*, 024906. [CrossRef]
20. Kolomeitsev, E.E.; Toneev, V.D.; Voronyuk, V. Vorticity and hyperon polarization at energies available at JINR Nuclotron-based Ion Collider fAcility. *Phys. Rev. C* **2018**, *97*, 064902. [CrossRef]
21. Wei, D.X.; Deng, W.T.; Huang, X.G. Thermal vorticity and spin polarization in heavy-ion collisions. *Phys. Rev. C* **2019**, *99*, 014905. [CrossRef]
22. Shi, S.; Li, K.; Liao, J. Searching for the subatomic swirls in the CuCu and CuAu collisions. *Phys. Lett. B* **2019**, *788*, 409–413. [CrossRef]
23. Vitiuk, O.; Bravina, L.V.; Zabrodin, E.E. Is different Λ and $\bar{\Lambda}$ polarization caused by different spatio-temporal freeze-out picture? *Phys. Lett. B* **2020**, *803*, 135298. [CrossRef]
24. Csernai, L.P.; Kapusta, J.I.; Welle, T. Λ and $\overline{\Lambda}$ spin interaction with meson fields generated by the baryon current in high energy nuclear collisions. *Phys. Rev. C* **2019**, *99*, 021901. [CrossRef]
25. Ivanov, Y.B. Global polarization in heavy-ion collisions based on the axial vortical effect. *Phys. Rev. C* **2020**, *102*, 044904. [CrossRef]
26. Voronyuk, V.; Kolomeitsev, E.E.; Tsegelnik, N.S. Hyperon global polarization in heavy-ion collisions at NICA energies. Feed-down effects and the role of Σ^0 hyperons. *arXiv* **2023**, arXiv:2305.10792.
27. Tsegelnik, N.S.; Kolomeitsev, E.E.; Voronyuk, V. Λ and $\overline{\Lambda}$ freeze-out distributions and global polarizations in Au + Au collisions. *Particles* **2023**, *6*, 373–384. [CrossRef]
28. Abgaryan, V.; Acevedo Kado, R.; Afanasyev, S.V.; Agakishiev, G.N.; Alpatov, E.; Altsybeev, G.; Alvarado Hernández, M.; Andreeva, S.V.; Andreeva, T.V.; Andronov, E.V.; et al. Status and initial physics performance studies of the MPD experiment at NICA. *Eur. Phys. J. A* **2022**, *58*, 140. [CrossRef]
29. Drnoyan, J.; Kolesnikov, V.; Mudrokh, A.; Vasendina, V.; Zinchenko, A. Perspectives of strangeness study at NICA/MPD from realistic Monte Carlo simulation. *Phys. Part. Nucl.* **2022**, *53*, 203–206. [CrossRef]
30. Nazarova, E.; Kolesnikov, V.; Parfenov, P.; Taranenko, A.; Teryaev, O.; Troshin, V.; Voronyuk, V.; Zinchenko, A. Performance study of the hyperon global polarization measurements with MPD at NICA. *Eur. Phys. J. A* **2024**, *60*, 85. [CrossRef]
31. Mudrokh, A. Prospects of the MPD Detector for Measuring the Spectra of Identified Hadrons in Bi + Bi Collisions at Energy $\sqrt{s_{NN}} = 9.2$ GeV. *Phys. Part. Nucl.* **2024**, *55*, 973–977. [CrossRef]
32. Bratkovskaya, E.L.; Cassing, W.; Konchakovski, V.P.; Linnyk, O. Parton-hadron-string dynamics at relativistic collider energies. *Nucl Phys. A* **2011**, *856*, 162–182. [CrossRef]
33. Cassing, W.; Tolos, L.; Bratkovskaya, E.L.; Ramos, A. Antikaon production in A+A collisions at SIS energies within an off-shell G-matrix approach. *Nucl. Phys. A* **2003**, *727*, 59–94. [CrossRef]
34. Tsegelnik, N.S.; Kolomeitsev, E.E.; Voronyuk, V. Helicity and vorticity in heavy-ion collisions at energies available at the JINR Nuclotron-based Ion Collider facility. *Phys. Rev. C* **2023**, *107*, 034906. [CrossRef]
35. Miller, M.L.; Reygers, K.; Sanders, S.J.; Steinberg, P. Glauber Modeling in High-Energy Nuclear Collisions. *Ann. Rev. Nucl. Part. Sci.* **2007**, *57*, 205–243. [CrossRef]
36. Adamczyk, L.; Agakishiev, G.; Aggarwal, M.M.; Ahammed, Z.; Alakhverdyants, A.V.; Alekseev, I.; Alford, J.; Anderson, B.D.; Anson, C.D.; Arkhipkin, D.; et al. Inclusive charged hadron elliptic flow in Au + Au collisions at $\sqrt{s_{NN}} = 7.7$–39 GeV. *Phys. Rev. C* **2012**, *86*, 054908. [CrossRef]
37. Abelev, B.; Adam, J.; Adamová, D.; Adare, A.M.; Aggarwal, M.M.; Aglieri Rinella, G.; Agnello, M.; Agocs, A.G.; Agostinelli, A.; Ahammed, Z.; et al. Centrality determination of Pb-Pb collisions at $\sqrt{s_{NN}} = 2.76$ TeV with ALICE. *Phys. Rev. C* **2013**, *88*, 044909. [CrossRef]
38. Zherebtsova, E.; Klochkov, V.; Selyuzhenkov, I.; Taranenko, A.; Kashirin, E. Procedure for event characterization in Pb-Pb collisions at 40AGeV in the NA49 experiment at the CERN SPS. *EPJ Web Conf.* **2018**, *182*, 02132. [CrossRef]

39. Klochkov, V.; Selyuzhenkov, I. Centrality determination in heavy-ion collisions with the CBM experiment. *J. Phys. Conf. Ser.* **2017**, *798*, 012059. [CrossRef]
40. Das, S.J.; Giacalone, G.; Monard, P.A.; Ollitrault, J.Y. Relating centrality to impact parameter in nucleus-nucleus collisions. *Phys. Rev. C* **2018**, *97*, 014905. [CrossRef]
41. Rogly, R.; Giacalone, G.; Ollitrault, J.Y. Reconstructing the impact parameter of proton-nucleus and nucleus-nucleus collisions. *Phys. Rev. C* **2018**, *98*, 024902. [CrossRef]
42. Segal, I.; Taranenko, A.; Golosov, O.; Parfenov, P.; Idrisov, D. Possibilities of using different estimators for centrality determination with the BM@N experiment. *Phys. At. Nucl.* **2023**, *86*, 1502–1507. [CrossRef]
43. Parfenov, P.; Idrisov, D.; Luong, V.B.; Taranenko, A. Relating charged particle multiplicity to impact parameter in heavy-ion collisions at NICA energies. *Particles* **2021**, *4*, 275–287. [CrossRef]
44. Segal, I.; Taranenko, A. The impact of the fragmentation processes of spectators on the centrality determination in heavy-ion collisions. *Phys. Part. Nucl.* **2024**, *55*, 1129–1133. [CrossRef]
45. Cassing, W.; Bratkovskaya, E.L. Hadronic and electromagnetic probes of hot and dense nuclear matter. *Phys. Rept.* **1999**, *308*, 65–233. [CrossRef]
46. Cassing, W.; Palmese, A.; Moreau, P.; Bratkovskaya, E.L. Chiral symmetry restoration versus deconfinement in heavy-ion collisions at high baryon density. *Phys. Rev. C* **2016**, *93*, 014902. [CrossRef]
47. Palmese, A.; Cassing, W.; Seifert, E.; Steinert, T.; Moreau, P.; Bratkovskaya, E.L. Chiral symmetry restoration in heavy-ion collisions at intermediate energies. *Phys. Rev. C* **2016**, *94*, 044912. [CrossRef]
48. Nilsson-Almqvist, B.; Stenlund, E. Interactions between hadrons and nuclei: The Lund Monte Carlo—FRITIOF version 1.6. *Comp. Phys. Comm.* **1987**, *43*, 387–397. [CrossRef]
49. Andersson, B.; Gustafson, G.; Pi, H. The FRITIOF model for very high-energy hadronic collisions. *Z. Phys. C* **1993**, *57*, 485–494. [CrossRef]
50. Alt, C.; Anticic, T.; Baatar, B.; Barna, D.; Bartke, J.; Betev, L.; Białkowska, H.; Blume, C.; Boimska, B.; Botje, M.; et al. Energy dependence of Λ and Ξ production in central Pb + Pb collisions at 20A, 30A, 40A, 80A, and 158A GeV measured at the CERN Super Proton Synchrotron. *Phys. Rev. C* **2008**, *78*, 034918. [CrossRef]
51. Alt, C.; Anticic, T.; Baatar, B.; Barna, D.; Bartke, J.; Betev, L.; Białkowska, H.; Billmeier, A.; Blume, C.; Boimska, B.; et al. Ω^- and $\overline{\Omega}^+$ production in central Pb + Pb collisions at 40 and 158 A GeV. *Phys. Rev. Lett.* **2005**, *94*, 192301. [CrossRef] [PubMed]
52. Koch, P.; Muller, B.; Rafelski, J. Strangeness in Relativistic Heavy Ion Collisions. *Phys. Rept.* **1986**, *142*, 167–262. [CrossRef]
53. Zeeb, G.; Reiter, M.; Bleicher, M. Multistrange baryon production in Au + Au collisions near threshold. *Phys. Lett. B* **2004**, *586*, 297–302. [CrossRef]
54. Arakelyan, G.H.; Merino, C.; Shabelski, Y.M. Multistrange hyperon production on nuclear targets. *Phys. Rev. D* **2022**, *105*, 114013. [CrossRef]
55. Amelin, N.S.; Gudima, K.K.; Toneev, V.D. Quark–Gluon String Model and Ultrarelativistic Heavy Ion Interactions. *Sov. J. Nucl. Phys.* **1990**, *51*, 327–333.
56. Amelin, N.S.; Gudima, K.K.; Toneev, V.D. Ultrarelativistic nucleus-nucleus collisions within a dynamical model of independent quark-gluon strings. *Sov. J. Nucl. Phys.* **1990**, *51*, 1093–1101.
57. Amelin, N.S.; Gudima, K.K.; Sivoklokov, S.Y.; Toneev, V.D. Further Development of a Quark–Gluon String Model for Describing High-energy Collisions With a Nuclear Target. *Sov. J. Nucl. Phys.* **1990**, *52*, 172–178.
58. Adam, J.; Adamczyk, L.; Adams, J.R.; Adkins, J.K.; Agakishiev, G.; Aggarwal, M.M.; Ahammed, Z.; Alekseev, I.; Anderson, D.M.; Aoyama, R.; et al. Strange hadron production in Au + Au collisions at $\sqrt{s_{NN}} = 7.7$, 11.5, 19.6, 27, and 39 GeV. *Phys. Rev. C* **2020**, *102*, 034909. [CrossRef]
59. Schnedermann, E.; Sollfrank, J.; Heinz, U.W. Fireball spectra. *NATO Sci. Ser. B* **1993**, *303*, 175–206.
60. Schnedermann, E.; Sollfrank, J.; Heinz, U.W. Thermal phenomenology of hadrons from 200-A/GeV S+S collisions. *Phys. Rev. C* **1993**, *48*, 2462–2475. [CrossRef]
61. Becattini, F.; Inghirami, G.; Rolando, V.; Beraudo, A.; Del Zanna, L.; De Pace, A.; Nardi, M.; Pagliara, G.; Chandra, V. A study of vorticity formation in high energy nuclear collisions. *Eur. Phys. J. C* **2015**, *75*, 406; Erratum in *Eur. Phys. J. C* **2018**, *78*, 354. [CrossRef]
62. Moreau, P.; Soloveva, O.; Oliva, L.; Song, T.; Cassing, W.; Bratkovskaya, E. Exploring the partonic phase at finite chemical potential within an extended off-shell transport approach. *Phys. Rev. C* **2019**, *100*, 014911. [CrossRef]
63. Voronyuk, V.; Kolomeitsev, E.E.; Kolomoyets, N.V.; Teryaev, O.V.; Tsegelnik, N.S. The Hubble constant in heavy-ion collisions. *Phys. Part. Nucl.* **2024**, *55*, 968–972. [CrossRef]
64. Lisa, M.; Ajitanand, N.; Alexander, J.; Anderson, M.; Best, D.; Brady, F.; Case, T.; Caskey, W.; Cebra, D.; Chance, J.; et al. Azimuthal dependence of pion interferometry at the AGS. *Phys. Lett. B* **2000**, *496*, 1–8. [CrossRef]
65. Lisa, M.A.; Heinz, U.W.; Wiedemann, U.A. Tilted pion sources from azimuthally sensitive HBT interferometry. *Phys. Lett. B* **2000**, *489*, 287–292. [CrossRef]
66. Ivanov, Y.B.; Soldatov, A.A. Vortex rings in fragmentation regions in heavy-ion collisions at $\sqrt{s_{NN}} = 39$ GeV. *Phys. Rev. C* **2018**, *97*, 044915. [CrossRef]
67. Kundu, P.K.; Cohen, I.M. *Fluid Mechanics*, 2nd ed.; Academic Press: San Diego, CA, USA, 2002.
68. Biermann, L. Über den Ursprung der Magnetfelder auf Sternen und im interstellaren Raum. *Z. Naturforschung Teil A* **1950**, *5*, 65.

69. Rogachevsky, O.V.; Sorin, A.S.; Teryaev, O.V. Chiral vortaic effect and neutron asymmetries in heavy-ion collisions. *Phys. Rev. C* **2010**, *82*, 054910. [CrossRef]
70. Baznat, M.; Gudima, K.; Sorin, A.S.; Teryaev, O.V. Helicity separation in heavy-ion collisions. *Phys. Rev. C* **2013**, *88*, 061901. [CrossRef]

Disclaimer/Publisher's Note: The statements, opinions and data contained in all publications are solely those of the individual author(s) and contributor(s) and not of MDPI and/or the editor(s). MDPI and/or the editor(s) disclaim responsibility for any injury to people or property resulting from any ideas, methods, instructions or products referred to in the content.